Supplement of Geosci. Model Dev., 19, 6857–6878, 2026
https://doi.org/10.5194/gmd-19-6857-2026-supplement

Geoscientific Model Development
Open Access

Supplement of

MErSiM v1.0: resolving biases in global silicate weathering model with a data-driven surface erosion module

Jiaxi Zhao et al.

Correspondence to: Yonggang Liu (ygliu@pku.edu.cn)

More details on the methods and data used in this study, and eight supplemental figures are provided below.

Sect. S1 ADDITIONAL DETAILS ON METHODS

Sect. S1.1 Mechanisms for calculating denudation rates using ^{10}Be

OCTOPUS is a dataset that has calculated denudation rates based on in-situ Beryllium 10 isotope (^{10}Be) for over 4,000 river basins, spanning various tectonic and climatic environments (Codilean et al., 2018). ^{10}Be, having a half-life of 1.39×10^6 years, is a kind of cosmogenic radionuclides (CRN) generated in the Earth's atmosphere and then falls out onto the ground. The ^{10}Be concentration in the sediments is highly dependent on the surface productivity and denudation rate at the site (Von Blanckenburg and Willenbring, 2014). Subsequently, it is carried out through hillslope processes to the stream system, where eroded sediment is mixed and transported throughout the watershed in a relatively short time period ($< 10^3$ years) (Dietrich and Dunne, 1978; Kelsey et al., 1987). Therefore, the average sediment ^{10}Be concentration at the outlet can be used as a measure of the average denudation rate in the catchment (Granger and Schaller, 2014). This method avoids the temporal variability and human impacts existing in sediment loading measurement (Kirchner et al., 2001), and escapes the inherent bias of thermochronologic technique that overestimates recent erosion rates by clipping the unmeasurable slow ones (Herman et al., 2013).

We combine the global (CRN Global collection: River basins) and Australian (CRN Australian collection: River basins) data from the database to obtain a complete dataset (4116 entries) covering the major river basins around the world. This allows us to compare changes in denudation rates under vastly different tectonic and climatic settings. Note that the basin sizes are drastically different, as small as 0.01 km^2, and as large as 70936 km^2. The median basin area is approximately 42 km^2, and the average basin area is 1508 km^2, with many catchments spanning tens to hundreds of square kilometers.

Sect. S1.2 The machine learning methods and cross validation

To build up reliable models for predicting the (logarithmic) global denudation rates, we compare the different approaches, including multivariate linear regression, neural network, support vector machine (SVM), decision tree, gradient boosting, random forest in R. We evaluate the performance of models by comparing the Root Mean Squared Error (RMSE) and the coefficient of determination (R^2). The results of model predictions are shown in Figure S3. RMSE is calculated according to

$$\mathrm{RMSE} = \sqrt{\frac{1}{n}\sum_{i=1}^{n}(y_i - \hat{y}_i)^2} \qquad \text{(S1)}$$

where y_i is the actual value, $\hat{y}_i$ is the predicted value, and n is the sample size. R^2 is a statistical measure that assesses the goodness of fit of a linear regression model to observed data. Its value ranges from 0 to 1, where a value closer to 1 indicates a better fit. The formula for calculating R^2 is:

$$R^2 = 1 - \frac{\text{sum squared regression (SSR)}}{\text{total sum of squares (SST)}} = 1 - \frac{\sum(y_i - \hat{y}_i)^2}{\sum(y_i - \bar{y})^2} \qquad \text{(S2)}$$

Neither the multivariate linear regression and the neural network method does a great job in predicating the denudation rates for the basins that have ^{10}Be measurements as described above. The former method is mainly used to describe the linear relationship between explanatory variables and dependent variables. Because of the high nonlinearity, this method could reach a minimum RMSE of only 1.85 and R^2 of 0.45. The neural network method is inspired by the structure and function of the human brain, which consists of a large number of interconnected nodes that can process and analyze data. However, it shows no specific advantage in dealing with this relatively small tabular dataset, as it shows R^2 of 0.73 on the validation set when we train the model with the 'nnet' package in R.

The Support Vector Machine (SVM) method uses a kernel function to project the input features into a high-dimensional feature space, thus converting linearly indivisible features into divisible ones, and iteratively adjusting the hyperplane to find the optimal solution. This method performs better than the multivariate linear regression and the neural network method; the optimal SVM model trained with the 'e1071' package gives an RMSE of 0.88 and an R^2 of 0.77.

Decision tree regression is a machine learning model based on a tree structure, where the model divides the dataset top-down by selecting the best features and corresponding split points, and the splitting process is determined by maximizing or minimizing an evaluation criterion (e.g., mean square error). We use the 'rpart' package in R to train the decision tree (Therneau et al., 2012). The main hyperparameters of the decision tree model are complexity parameter (cp), minsplit, and maxdepth. cp is a hyperparameter used for pruning to avoid overfitting; minsplit is the minimum number of samples that a node must have before it can be considered for splitting, a larger minsplit will result in a simpler model; maxdepth determines the maximum depth of the tree where deeper trees can capture more details of the data, but can also lead to overfitting. The value of cp is determined first by fixing minsplit and maxdepth to their default values. A final value of 0.004 is chosen as reducing cp does not result in a significant decrease in the relative error (see Fig. S11). The optimal hyperparameter combination of minsplit and maxdeption is then searched over the hyperparameter space, where minsplit is an integer from 10 to 30 and maxdepth is an integer from 5 to 15. During the searching, 10-fold cross-validation is used to reduce the systematic sampling bias. The optimal combination is found to be (minsplit = 18, maxdepth = 13, cp = 0.004). The decision tree model is then trained with this combination of hyperparameters and its results are displayed in Fig. 4 of the main text. This model has an RMSE of 1.12 and R^2 of 0.62 on the validation set.

Ensemble techniques, such as boosting, bagging enhance decision tree model's capacity to generalize by integrating the outputs of various trees. The boosting method, such as that used in the gradient boosting model, iteratively train on a dataset and modify the weights of the samples based on their error rates, until a predetermined number of trees is reached. The bagging method, on the other hand, randomly sample the dataset for each tree and foster multiple independent results. One popular model applying the bagging method is the random forest model. This model further improves its performance by selecting a subset of the features each time to reduce multicollinearity. We train the gradient boosting model with ‘gbm’ package (RMSE = 1.07, R^2 = 0.66) and random forest model with ‘randomForest’ package (RMSE = 0.73, R^2 = 0.85) (Liaw and Wiener, 2002) of R, with the latter obviously having a better performance.

Since the random forest model performs by far the best among all the models, it is chosen to predict the global denudation rates. The random forest model has its own hyperparameters that can be tuned to further improve the performance. This process is done on GEE. The main hyperparameters are numberOfTrees, minLeafPopulation (the minimum number of samples within a terminal node), and bagFraction (fraction of samples in the bag). A five-fold cross-validation is carried out to traverse the parameter space, and the optimal combination is found to be (numberOfTrees = 500, minLeafPopulation = 1, bagFraction = 0.9), which gives an RMSE of 0.691 and R^2 of 0.865 on the validation set. The random forest model with this optimal combination of hyperparameters is then trained for 100 times, each time involving a 5-fold cross-validation. The results of the 100 random runs are similar to each other, with the RMSE varying by less than 0.01, indicating that the model is stable.

The importance of each predictor or feature variable is ranked based on the TreeSHAP method. TreeSHAP is a variant of SHAP (SHapley Additive exPlanations, from coalitional game theory) for tree-based machine learning models. TreeSHAP values of each feature are the change in the expected model prediction due to that feature. Specifically, it is the average change in the model's output when this feature is varied over all possible values, while keeping all other features constant.

Sect. S1.3 Additional diagnostics for mafic lithologies and model scope

Our optimization objective was to minimize the discrepancy between simulated weathering flux and the 81 river basin observations from Gaillardet et al. (1999) and HYBAM, where no basaltic weathering basins are included. Nevertheless, MErSiM v1.0 includes basic volcanic rock (VB) in the mafic lithology class, and the mafic class has the largest Ca+Mg concentration proportionality constant (k_d) of 10317 mol

m^{-3} compared to other 5 lithologies. k_d scales the chemical dissolution rate K, which depends on both runoff and temperature.

$$K = k_d(1 - e^{-k_w q})\, e^{\left[\left(\frac{E_a}{R}\right)\left(\frac{1}{T_0} - \frac{1}{T}\right)\right]}$$

This parameterization permits a higher contribution of basaltic rock to the global silicate weathering Ca+Mg flux. Because the dependence of dissolution rate *K* on runoff *q* and temperature *T* is scaled by k_d , the model retains the climatic controls emphasized by Dessert et al. (2003). Therefore, MErSiM includes basaltic/mafic lithologies in the global Ca+Mg calculation.

A diagnostic calculation shows that VB covers 4.82×10^6 km^2 (3.77% of lithology-classified land area) and contributes 0.78×10^{12} mol yr^{-1} (25.0% of the global MErSiM Ca+Mg flux). The broader mafic group (basic volcanic rock + basic plutonic rock, VB+PB) contributes 0.94×10^{12} mol yr^{-1} (30.3%). The basaltic rock contribution in MErSiM Ca+Mg flux is surprisingly similar to the estimate of the basaltic rock contribution in global CO_2 consumption flux (30% - 35%) of Dessert et al. (2003), even though they have used a different modeling scheme.

We also checked the erosion model. In the training dataset, the propotion of basic volcanic rock (ROCK=2) is quite limited as the reviewer has noticed: 62 of 3706 basin samples (1.67%), but it has not been completely neglected. The erosion-rate distribution of these samples is highly skewed, with a median of 11.4 mm kyr^{-1} and a mean of 123 mm kyr^{-1} because a small number of high-erosion settings raise the average. This supports a more precise statement: the erosion model is not blind to basic volcanic terrains, but the basaltic subset is small and should not be overinterpreted as a complete representation of island basalt weathering with fast erosion.

Although basaltic rocks are included through the lithology map and the mafic parameter, MErSiM v1.0 does not include a separate basalt-weathering law. Specifically, Dessert et al. (2003) compiled several small basaltic catchments and volcanic provinces, found that basaltic rivers have high Ca/Na, Mg/Na, and HCO3/Na ratios, and proposed a strong runoff-temperature control on basalt weathering. They have used regression method and found that the specific atmospheric CO_2 consumption rate f_{CO_2} (mol km^{-2} yr^{-1}), is

$$f_{CO_2} = R_f \times 323.44e^{0.0642T}$$

Where R_f is runoff (mm/yr) and T is temperature (°C), with a regression $R^2 = 0.7$. The weathering scheme we have adopted in MErSiM v1.0 is from Gabet and Mudd (2009), which has used the compilation of weathering flux from West et al. (2005). This compilation did not include basalt-bearing watersheds. Therefore, we conducted several analysis to see whether this transport/kinetics-limited model framework could, to some extent, describe the characteristics of basalt weathering observed by Dessert et al. (2003).

We analyzed the weathering fluxes simulated by the MErSiM model and found that in areas with basaltic rock, the simulated weathering fluxes could be described by the product of the runoff and temperature exponential functions, with an R^2 of 0.65 (Figure S6).

$$f_{VB} = R_f \times 239.35e^{0.0461T}$$

This is consistent with the relationship established by Dessert et al. (2003) based on data from a dozen river basins, including the Columbia Plateau and the Deccan Traps, though it should not be interpreted as a direct reproduction of their basalt CO_2-consumption law. Specifically, the fitted coefficients for VB (0.0461 and 239.35) are lower than those of Dessert et al. (2003). This may be because they have used the number of moles of bicarbonate, whereas our model only accounts for the number of moles of Ca and Mg cations. However, we still note that the order of magnitude of these constants is consistent with the results of Dessert et al. (2003). In contrast, weathering fluxes in granite cannot be well described by this relationship with an R^2 of 0.33 (Figure S6), and the sensitivity constants are significantly smaller than basalts (0.0299 and 36.15), highlighting a stronger dependence of basalt weathering on climate.

We also found that in general, weathering flux increases with erosion rate for both basalt and granite (Figure S7). When the erosion rate does not exceed 100 mm/kyr, a significant number of weathering flux are clearly limited by the erosion rate.

Our frequency analysis of basalt erosion rates revealed that, while a considerable number of basalt regions indeed have erosion rates around 100 mm/kyr (in contrast, granite erosion rates are widely distributed around 30 mm/kyr), low-erosion zones with rates around 10 mm/kyr are equally prevalent (Figure S8), as areas with gentle slopes and low tectonic activity account for a large proportion of the continent's land area. In other words, although many oceanic islands are located in tectonically active zones with mountainous topography and high physical erosion rates—where the supply of fresh rock is not a bottleneck—not all basalt weathering occurs within the kinetics-limited regime. For example, the erosion rates of the Karoo basalt in South Africa's semi-arid, flat areas are extremely low, generally < 4 mm/kyr (Decker et al., 2013). Therefore, island basalt and continental basalt may not be treated as equivalent, as Li and Elderfield (2013) has suggested when they were trying to estimate the CO_2 consuming rate of continental weathering.

Moreover, even some of the island basalt weathering is constrained by erosion. The erosion module in MErSiM yields lower erosion rates for tropical islands compared to

Park et al.(2020) (Figure 5d in the manuscript). The role of basalt in carbon consumption in Southeast Asia emphasized by Park et al. (2020) is partly because basalt is assigned a high dissolution rate in weathering calculations, and partly because their SPIM model highlights the effects of large runoff on erosion rate in these tropical islands. Park et al. (2020) proposed that enhancement of Southeast Asian mafic island weathering was a driver of Neogene cooling, but this increasing flux of unradiogenic mafic is not reconciled with the trend toward more radiogenic Sr and Os isotope values (Caves Rugenstein et al., 2021).

In summary, although the MErSiM v1.0 weathering model framework does not perform separate calculations for basalt weathering, the results still highlight the significant climate dependence of basalt weathering. This dependency is distinguished from other rock types, and to some extent align with the relationship between basalt weathering flux and temperature/runoff identified by Dessert et al. (2003). At the same time, the MErSiM model framework can also depict the weathering-erosion relationship. A large portion of the basalt weathering basins are still limited by the supply of fresh material. Note that physical erosion is a factor that Dessert et al. (2003) did not discuss, perhaps because the basalt weathering regions lacked field-measured erosion rate data (as mentioned above, samples with beryllium isotope erosion rates from basalt weathering basins are very limited). While cosmogenic ^{10}Be measurements are generally unavailable for basaltic terrains due to the scarcity of quartz, recent methodological advances have enabled the use of cosmogenic ^{36}Cl in detrital magnetite to quantify watershed-averaged denudation rates (Moore and Granger, 2019; Moore et al., 2024). These approaches may offer valuable constraints for future model-data comparisons in basaltic settings.

Sect. S2 SUPPLEMENTAL FIGURES

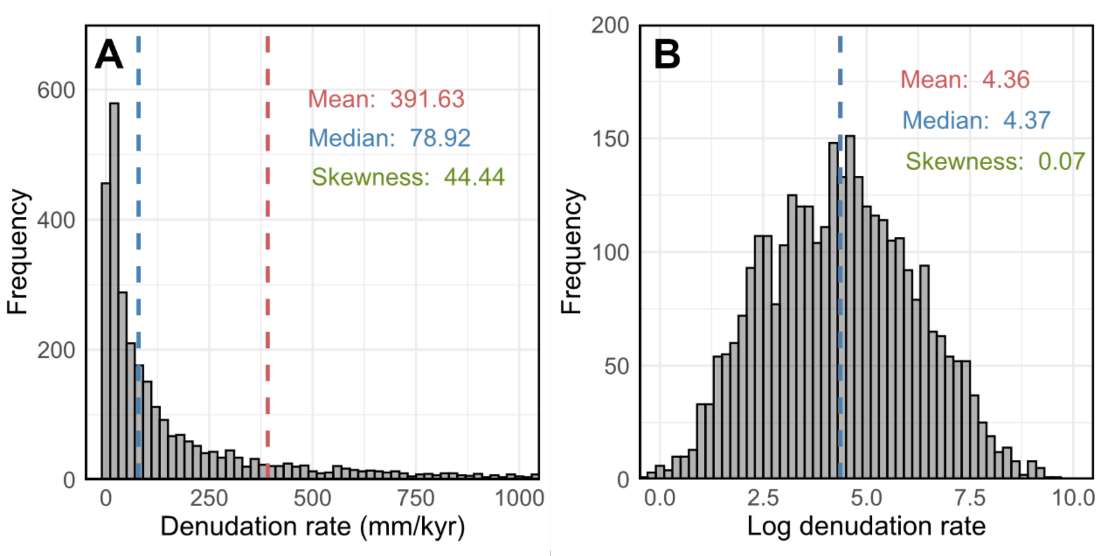

Fig. S1 (A) Histogram of denudation rates of 3967 river basins from OCTOPUS dataset, and the statistics. (B) Histogram of the logarithm of denudation rates in (A), note that it's much more closer to a normal distribution.

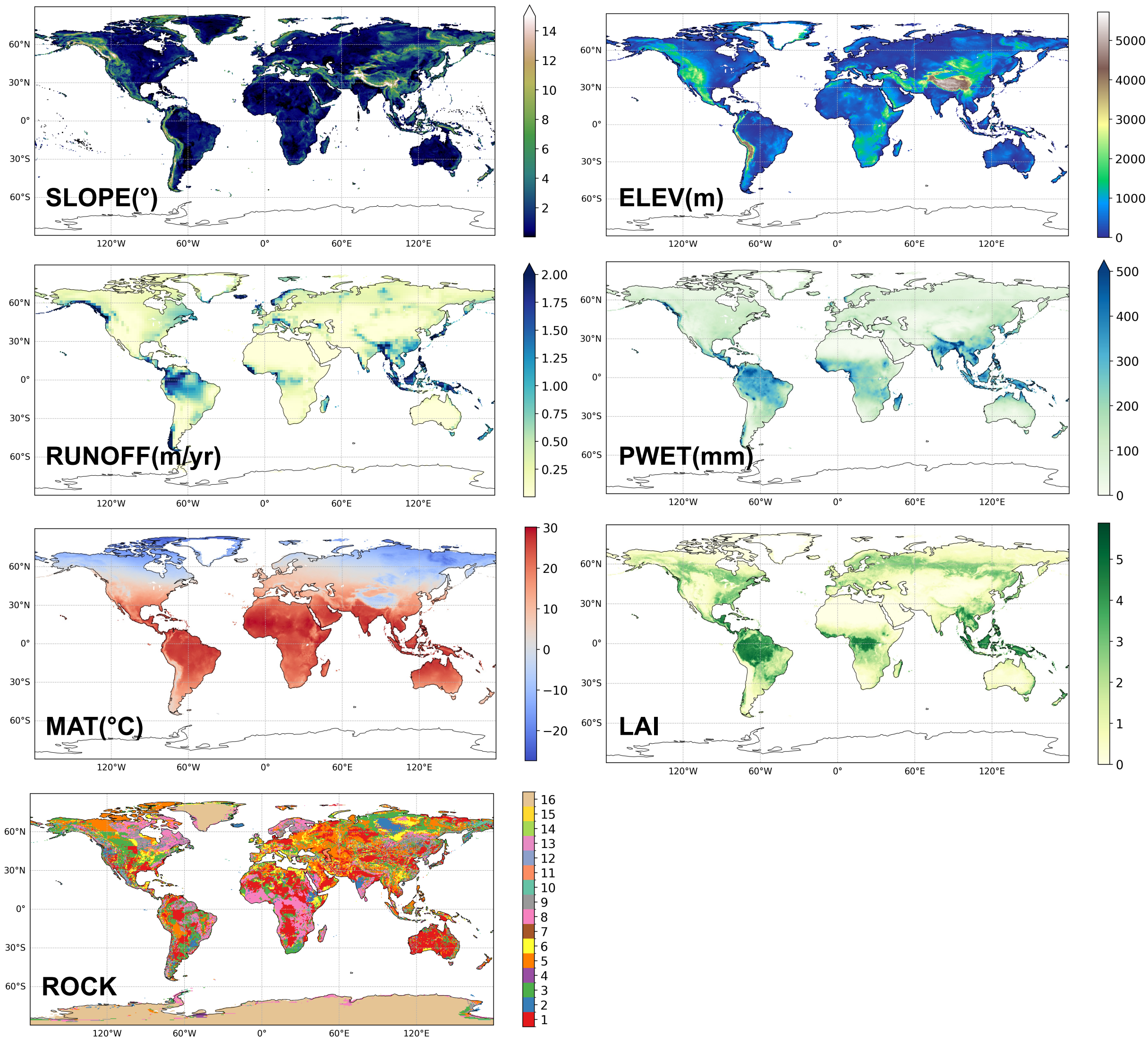

Fig. S2 Global distribution of 7 feature variables. All data is interpolated to the same $0.5° \times 0.5°$ spatial resolution.

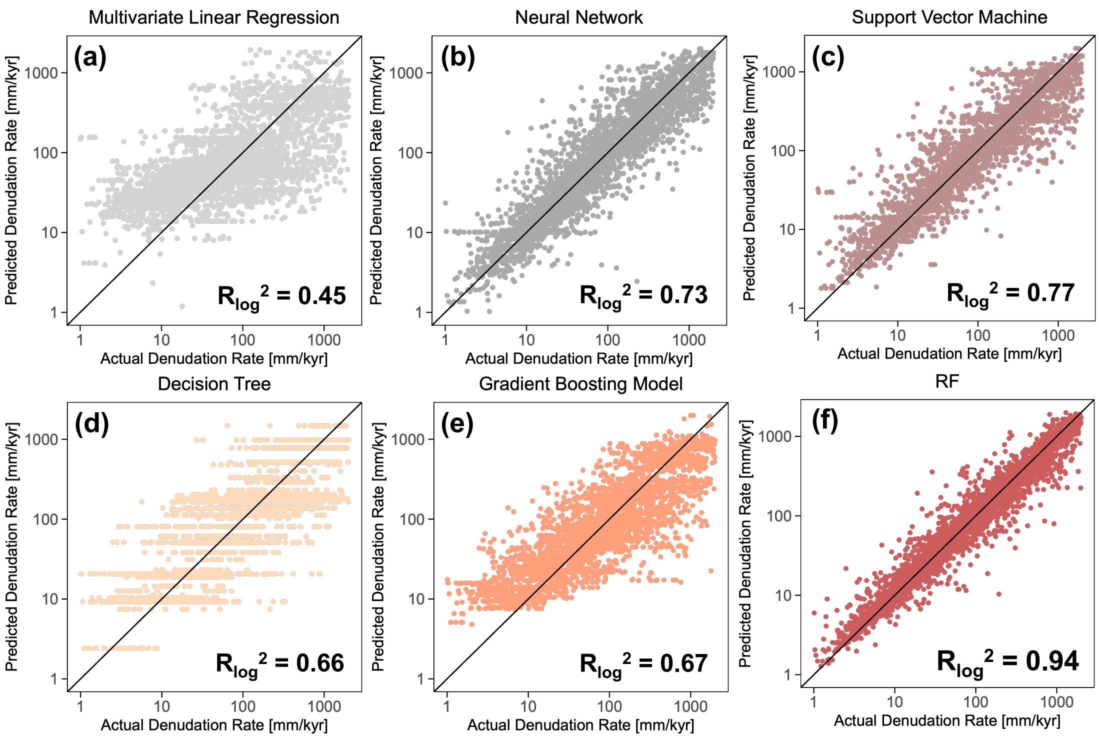

Fig. S3 Scatter of predicted basin denudation rates by different machine learning methods vs. observations from OCTOPUS. The observed erosion rates are plotted against the model-predicted rates (y-axis) for (a) Multivariate Linear Regression, (b) Neural Network, (c) Support Vector Machine, (d) Decision Tree, (e) Gradient Boosting Model, and (f) Random Forest. All models have been searched through the parameter space to get the optimal results. The diagonal line represents the 1:1 relationship. Both axes are on a logarithmic scale to accommodate the multi-order-of-magnitude range of erosion rates observed globally. The coefficient of determination for the logarithmic values (R_{log}^2) is used as the primary metric of performance, indicating the proportion of variance in the observed data that is explained by the model. All the inputs of these models are from the same compilation of basin-average variable values.

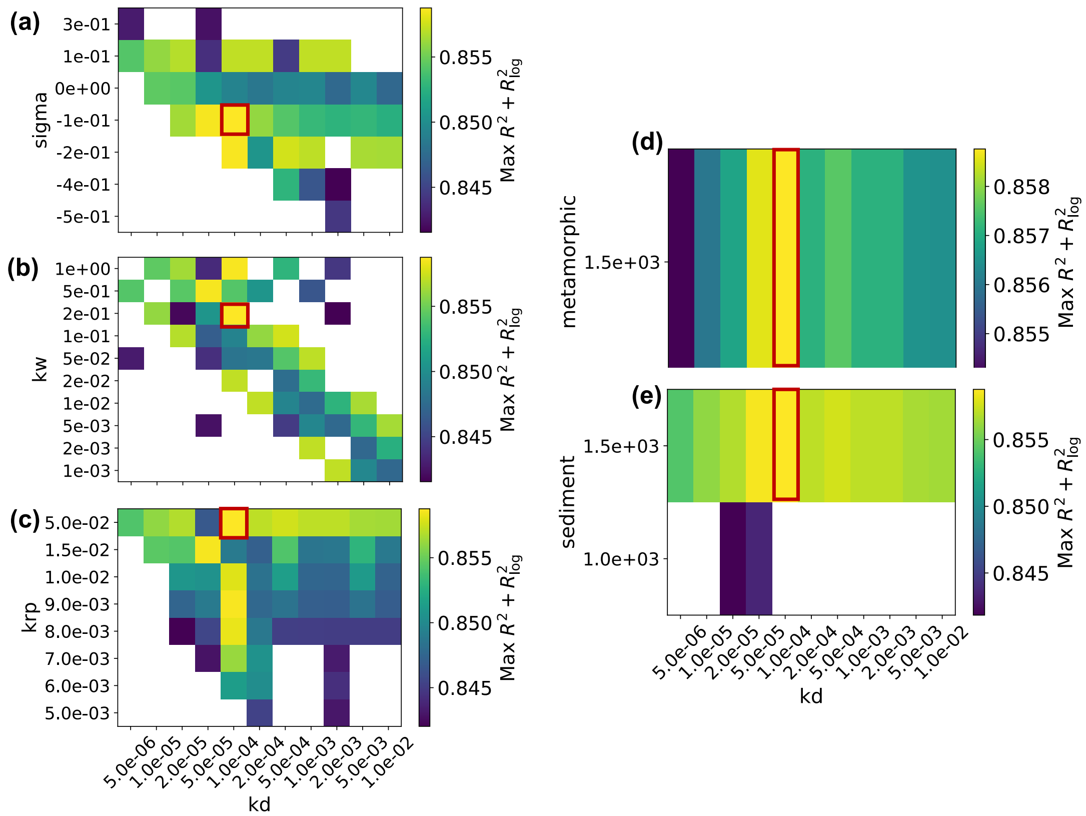

Fig. S4 Parameter space sensitivity for the MErSiM model. The heatmaps show the maximum combined performance metric ($R^2 + R^2_{log}$) achieved across the parameter space (only 100 best parameter combinations are shown). Each panel displays the interaction between the base dissolution rate constant (k_d, x-axis) and another key parameter (y-axis): (a) the weathering time-exponent sigma (σ), (b) the runoff sensitivity k_w, (c) the regolith production rate k_{rp}, (d) the cation concentration for metamorphic rocks, and (e) the cation concentration for sediment. The color in each grid cell represents the highest $R^2 + R^2_{log}$ value obtained by varying all other unplotted parameters, while keeping the x- and y-axis parameters fixed. The red boxes highlight the region of the parameter space containing the optimal parameter set identified in our study (see Table 2). The well-defined, bright yellow "sweet spot" in these plots demonstrates that our calibration has converged on a robust and well-constrained optimal solution.

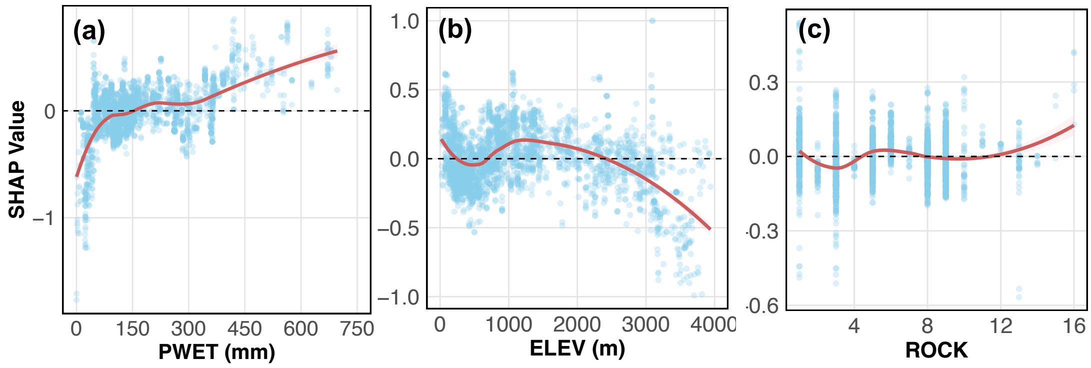

Fig. S5 SHAP dependence plots for predictor variables with lower feature importance: PWET, ELEV, and ROCK. Each plot shows the relationship between a feature's value (x-axis) and its corresponding SHAP value (y-axis) for every watershed in the training dataset. The SHAP value quantifies the feature's marginal contribution to the final logarithmic erosion rate prediction. The red line represents the smoothed average trend (LOESS). (a) For PWET, the model identifies a threshold of about 50 mm, below which insufficient PWET decrease erosion rates. (b) For ELEV (Elevation), there is a distinct negative impact at higher elevations (> 2500 m). This suggests the model has learned that high elevation does not guarantee high erosion, likely because many high-altitude regions are topographically gentle plateaus with low erosion rates. (c) For ROCK (Lithology), the SHAP values are tightly clustered around zero, confirming the low feature importance of lithology at the global scale.

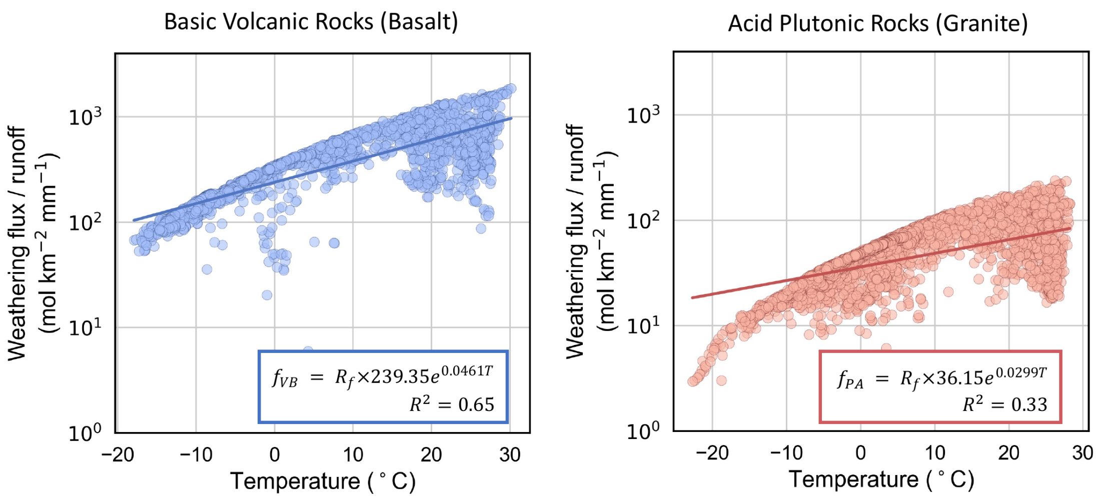

Fig. S6 Dessert-type relationship between weathering flux and climate. The y-axis represents the ratio of the simulated weathering flux per unit area to runoff. Blue indicates cells with basic volcanic rocks (VB), and red indicates cells with acidic plutonic rocks (PA). The fitted relationships are shown in the boxes.

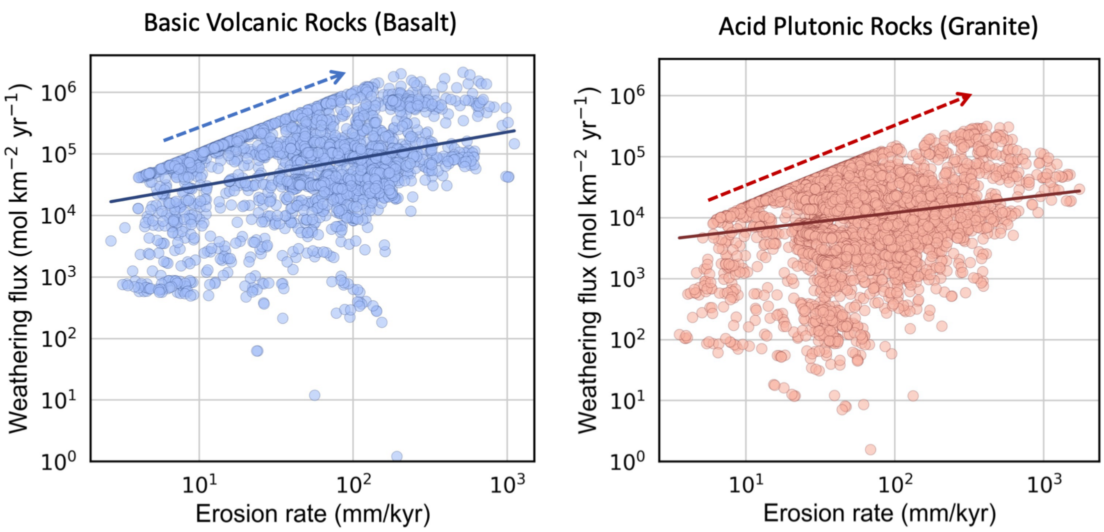

Fig. S7 Relationship between erosion rate and weathering flux for basic volcanic rocks (VB) and acidic plutonic rocks (PA). The fitted straight lines illustrate the power-law relationship. The dashed arrows indicate the limiting effect of erosion on weathering flux at low erosion rates.

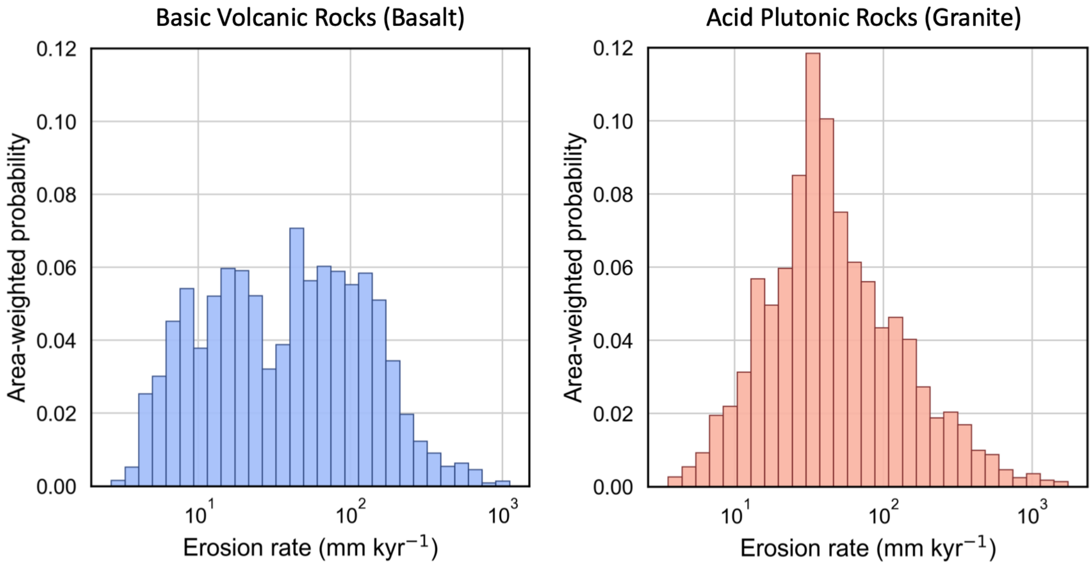

Fig. S8 Frequency distribution of erosion rates for basic volcanic rocks (VB) and acidic plutonic rocks (PA). Many VB cells occur at low-to-moderate erosion rates, indicating that continental basic volcanic terrain should not be treated as equivalent to small, high-erosion volcanic islands.

Table. S 1 7 predictors used for the random forest model

	Predictors	Description	Spatial resolution	Time span	Unit	source	Reference
Tectonic	SLOPE	Steepness of Earth Surface	1 arc second	\	°	Shuttle Radar Topography Mission (SRTM)	Farr et al., 2007 (https://doi.org/10.1029/2005RG000183)
	ELEV	Height of the Earth's Surface Relative to Mean Sea Level (MSL)			m		
	ROCK	Type of Bedrock	0.5° × 0.5°	\	\	Global Lithologic Map (GliM)	Hartmann and Moosdorf, 2012 (https://doi.org/10.1029/2012gc004370)
Climatic	MAT	Annual Mean Temperature	0.5° × 0.5°	1901-2013	°C	CRU TS v.4.03	Harris et al., 2014 (https://doi.org/10.1002/joc.3711)
	PWET	Precipitation of Wettest Month	1km	1970-2000	mm	WorldClim 2.1	Fick and Hijmans, 2017 (10.1002/joc.5086)
	RUNOFF	Annual Mean Runoff	0.5° × 0.5°	2016-2021	mm/yr	Geophysical Fluid Dynamics Laboratory (GFDL) CM2.0	Park et al., 2020 (https://doi.org/10.1073/pnas.2011033117)
Biotic	LAI	Leaf Area Index	0.5° × 0.5°	2001-2004	\	NCAR	Lawrence and Chase, 2007 (https://doi.org/10.1029/2006JG000168)

Table. S 2 15 categories of Lithology and their definitions

Number	ID	Lithology
1	PA	Acid Plutonic
2	VA	Acid Volcanic
3	PB	Basic Plutonic
4	VB	Basic Volcanic
5	SC	Carbonate Sedimentary rocks
6	EV	Evaporite
7	IG	Ice and Glaciers
8	PI	Intermediate Plutonics
9	VI	Intermediate Volcanics
10	MT	Metamophics
11	SM	Mixed Sedimentary rocks
12	PY	Pyroclastics
13	SS	Siliciclastic Sedimentary rocks
14	SU	Unconsolidated Sedimentary rocks
15	ND	Undefined

Sect. S3. ADDITIONAL REFERENCES CITED

Caves Rugenstein, J.K., Ibarra, D.E., Zhang, S., Planavsky, N.J., and Von Blanckenburg, F., 2021, Isotope mass-balance constraints preclude that mafic weathering drove Neogene cooling: Proceedings of the National Academy of Sciences, v. 118, p. e2026345118, doi:10.1073/pnas.2026345118.

Codilean, A.T., Munack, H., Cohen, T.J., Saktura, W.M., Gray, A., and Mudd, S.M., 2018, OCTOPUS: an open cosmogenic isotope and luminescence database: Earth System Science Data, v. 10, p. 2123–2139, doi:10.5194/essd-10-2123-2018.

Decker, J.E., Niedermann, S., and De Wit, M.J., 2013, Climatically influenced denudation rates of the southern African plateau: Clues to solving a geomorphic paradox: Geomorphology, v. 190, p. 48–60, doi:10.1016/j.geomorph.2013.02.007.

Dessert, C., Dupré, B., Gaillardet, J., François, L.M., and Allègre, C.J., 2003, Basalt weathering laws and the impact of basalt weathering on the global carbon cycle: Chemical Geology, v. 202, p. 257–273, doi:10.1016/j.chemgeo.2002.10.001.

Dietrich, W., and Dunne, T., 1978, Sediment Budget for a Small Catchment in Mountainous Terrain: Z. Geomorphol. Suppl., v. 29, doi:10.1130/0091-7613(2001)029.

Gabet, E.J., and Mudd, S.M., 2009, A theoretical model coupling chemical weathering rates with denudation rates: Geology, v. 37, p. 151–154, doi:10.1130/G25270A.1.

Gaillardet, J., Dupré, B., Louvat, P., and Allègre, C.J., 1999, Global silicate weathering and CO2 consumption rates deduced from the chemistry of large rivers: Chemical Geology, v. 159, p. 3–30, doi:10.1016/S0009-2541(99)00031-5.

Granger, D.E., and Schaller, M., 2014, Cosmogenic Nuclides and Erosion at the Watershed Scale: Elements, v. 10, p. 369–373, doi:10.2113/gselements.10.5.369.

Herman, F., Seward, D., Valla, P.G., Carter, A., Kohn, B., Willett, S.D., and Ehlers, T.A., 2013, Worldwide acceleration of mountain erosion under a cooling climate: Nature, v. 504, p. 423–426, doi:10.1038/nature12877.

Kelsey, H.M., Lamberson, R., and Madej, M.A., 1987, Stochastic model for the long-term transport of stored sediment in a river channel: Water Resources Research, v. 23, p. 1738–1750, doi:10.1029/WR023i009p01738.

Kirchner, J., Finkel, R., Riebe, C., Granger, D., Clayton, J., King, J., and Megahan, W., 2001, Mountain erosion over 10 yr, 10 k.y., and 10 m.y. time scales:

Geology, v. 29, doi:10.1130/0091-7613(2001)029<0591:MEOYKY>2.0.CO;2.

Li, G., and Elderfield, H., 2013, Evolution of carbon cycle over the past 100 million years: Geochimica et Cosmochimica Acta, v. 103, p. 11–25, doi:10.1016/j.gca.2012.10.014.

Liaw, A., and Wiener, M., 2002, Classification and Regression by randomForest: R News, v. 2, p. 18–22.

Moore, A.K., and Granger, D.E., 2019, Watershed-averaged denudation rates from cosmogenic 36Cl in detrital magnetite: Earth and Planetary Science Letters, v. 527, p. 115761, doi:10.1016/j.epsl.2019.115761.

Moore, A.K., Méndez Méndez, K., Hughes, K.S., and Granger, D.E., 2024, Volcanic Arc Weathering Rates in the Humid Tropics Controlled by the Interplay Between Physical Erosion and Precipitation: AGU Advances, v. 5, p. e2023AV001066, doi:10.1029/2023AV001066.

Park, Y., Maffre, P., Goddéris, Y., Macdonald, F.A., Anttila, E.S.C., and Swanson-Hysell, N.L., 2020, Emergence of the Southeast Asian islands as a driver for Neogene cooling: Proceedings of the National Academy of Sciences, v. 117, p. 25319–25326, doi:10.1073/pnas.2011033117.

Therneau, T., Atkinson, B., and Ripley, B., 2012, Rpart: Recursive Partitioning: v. 3.

Von Blanckenburg, F., and Willenbring, J.K., 2014, Cosmogenic Nuclides: Dates and Rates of Earth-Surface Change: Elements, v. 10, p. 341–346, doi:10.2113/gselements.10.5.341.

West, A., Galy, A., and Bickle, M., 2005, Tectonic and climatic controls on silicate weathering: Earth and Planetary Science Letters, v. 235, p. 211–228, doi:10.1016/j.epsl.2005.03.020.